Geofísica Internacional (2023) **62-3**: 543 - 561

Disturbances in the geomagnetic field, water level and atmospheric pressure associated with Mw ≥ 6.6 earthquakes in the South Atlantic Ocean

M.A. Arecco[1,2]*, P.A. Larocca[1], F.A. Oreiro[1,3], M.E. Fiore[1,3], L.A. Otero[4,5], M.F. Canero[3]

Abstract

This paper is aimed at studying disturbances in the geomagnetic field (GMF), water level (WL) and sea-level atmospheric pressure (AP) associated with Mw≥ 6.6 seismic events in the Scotia arch, in the South Atlantic. GMF records from observatories of the International Magnetic Observatory Network (INTERMAGNET), WL records from tide stations of the Intergovernmental Oceanographic Commission, and hourly AP records from databases of the Global Modeling and Assimilation Office of the National Aeronautics and Space Administration have been analyzed in the area under study. For the analysis of geomagnetic disturbances, the GMF horizontal component (H), which is more susceptible to variations, was considered. For the WL analysis, the discrepancy (residue) between the WL time series from tide stations and the predicted level of astronomical tides, for a 10-day period before and after the occurrence of each earthquake, was calculated. For the AP analysis, the variation of data gridded between 1 and 2 hours before and after the earthquake was calculated. The analysis of the geomagnetic data prior to the seismic event, using a high-pass filter and the wavelet method, showed: a) high energy ranges in all frequencies, even in very high ones; and b) oscillations in the filter with amplitude peaks of ± 0.2 nT, and with an anticipation and duration consistent with the wavelet method. As regards the WL residues calculated, there were oscillations in the largest amplitudes in the sensors located closest to the earthquake, thus, those large amplitudes corresponded to shorter times of arrival. The AP study showed a maximum followed by a local minimum within a range of ± 0.3 hPa around the location of the earthquake. While the GMF analysis anticipated seismic events within a range of 6-2 hours, the techniques used for WL and AP could detect Mw>7 earthquakes, associating them with the rising/falling surface of the sea. These three techniques can be used jointly to implement a prevention or early warning system for seismic events or related hazards such as tsunamis and/or seiches in the study region.

Key words: Earthquakes, Atmospheric pressure, Tsunamis, Horizontal component of the geomagnetic field, Sunspots.

Resumen

Este trabajo tiene como objetivo estudiar las perturbaciones en el campo geomagnético (GMF), nivel del agua (WL) y presión atmosférica a nivel del mar (AP) asociadas a eventos sísmicos Mw≥ 6.6 en el arco de Scotia, en el Atlántico Sur. Registros GMF de los observatorios de la Red Internacional de Observatorios Magnéticos (INTERMAGNET), registros WL de las estaciones de mareas de la Comisión Oceanográfica Intergubernamental y registros AP por hora de las bases de datos de la Oficina Global de Modelado y Asimilación de la Administración Nacional de Aeronáutica y el Espacio han sido analizadas en el área de estudio. Para el análisis de perturbaciones geomagnéticas se consideró la componente horizontal GMF, la cual es más susceptible a variaciones. Para el análisis WL, se calculó la discrepancia (residuo) entre la serie temporal WL de las estaciones de mareas y el nivel pronosticado de las mareas astronómicas, durante un período de 10 días antes y después de la ocurrencia de cada terremoto. Para el análisis AP se calculó la variación de los datos grillados entre 1 y 2 horas antes y después del sismo. El análisis de los datos geomagnéticos previos al evento sísmico, utilizando un filtro de paso alto y el método wavelet, mostró: a) altos rangos de energía en todas las frecuencias, incluso en las muy altas; y b) oscilaciones en el filtro con picos de amplitud de ± 0.2 nT, y con una anticipación y duración consistente con el método wavelet. En cuanto a los residuos WL calculados, hubo oscilaciones en las mayores amplitudes en los sensores ubicados más cerca del sismo, por lo que esas grandes amplitudes correspondieron a tiempos de llegada más cortos. El estudio AP mostró un máximo seguido de un

Palabras clave: Terremotos, Presión atmosférica, Tsunamis, Componente horizontal del campo geomagnético, Manchas solares.

Received: November 8, 2022; Accepted: June 23, 2023; Published on-line: July 1, 2023.

Editorial responsibility: Dr. Juan Esteban Hernández Quintero

* Corresponding author: M.A. Arecco marecco@fi.uba.ar
[1] Universidad de Buenos Aires, Facultad de Ingeniería, Instituto de Geodesia y Geofísica Aplicadas. Buenos Aires, Argentina.
[2] Universidad de la Defensa Nacional, Facultad de la Armada, Escuela de Ciencias del Mar, Buenos Aires, Argentina.
[3] Ministerio de Defensa, Servicio de Hidrografía Naval, Buenos Aires, Argentina.
[4] Universidad de la Defensa Nacional, Facultad de Ingeniería del Ejército, Buenos Aires, Argentina.
[5] Ministerio de Defensa, CITEDEF – CONICET, Villa Martelli, Argentina.

María Alejandra Arecco, Patricia Alejandra Larocca, Fernando Ariel Oreiro, Mónica María Elisa Fiore, Lidia Ana Otero y María Florencia Canero

https://doi.org/10.22201/igeof.2954436xe.2023.62.3.1440

mínimo local dentro de un rango de ± 0,3 hPa alrededor de la ubicación del terremoto. Mientras que el análisis GMF anticipó eventos sísmicos dentro de un rango de 6-2 horas, las técnicas utilizadas para WL y AP pudieron detectar terremotos Mw>7, asociándolos con la superficie ascendente/descendente del mar. Estas tres técnicas pueden ser utilizadas en conjunto para implementar un sistema de prevención o alerta temprana de eventos sísmicos o peligros relacionados tales como tsunamis y/o seiches en la región de estudio.

Introduction

The South Atlantic Ocean is one of the most active seismic regions in the world, with the Scotia Arc, which surrounds the Scotia and South Sandwich plates. The edges of this active set are represented by various types of margins. The North Scotia Ridge, which extends from Tierra del Fuego, through the Burdwood/Namuncurá Bank, up to the Georgias del Sur Islands, is mainly represented by a transcurrent and convergent margin. This ridge separates the Scotia and Sandwich plates from the South American plate. The eastern edge of the Sandwich plate, represented by the volcanic arc of the Sandwich del Sur Islands, has a convergent margin, mainly developed from N to S by the South Sandwich Trench, which separates it from the South American plate. The western edge of the Scotia plate is represented by the Shackleton Fracture Zone beneath the Drake Passage. The southern edge of the Scotia and Sandwich plates is represented by a mixed transcurrent and accretionary margin, separating it from the Antarctic plate. This margin goes through the South Scotia Ridge, Elephant Island and the Orcadas del Sur Islands up to the southern South Sandwich arc.

The activity is represented by the displacement of the Antarctic plate moving eastwards with respect to the Scotia plate at a rate of around 6 mm/year, and the South American plate subducting beneath the South Sandwich microplate at a rate of around 70 to 80 mm/year. In this region, within one year, there may be over 300 seismic events with a moment magnitude (hereinafter M_w) of M_w>4, and at least one M_w>7 earthquake (Larocca *et al.*, 2019; 2021). The North Scotia Ridge, even though it is less active than the South Ridge, has around 20 M_w>4 earthquakes in a year (Figure 1).

One of the most elusive objectives of seismology is predicting earthquakes in the short term. There are numerous studies reporting associations between earthquakes and physical phenomena, such as electromagnetic field variations (Varotsos *et al.*, 2013; Hayakawa *et al.*, 2010; Takeuchi *et al.*, 2012; Gao *et al.*, 2014; Zhao *et al.*, 2021), anomalous GMF records on the earth's surface (Ruiz *et al.*, 2011; Takla *et al.*, 2018; Arecco *et al.*, 2020; Larocca *et al.*, 2021) or very low frequency changes in the electromagnetic field (Hayakawa *et al.*, 2010; Sierra Figueredo *et al.*, 2020). In addition, Thomas and Juárez (2021) reported significant mechanical effects in the focal region of an earthquake, namely deformation of rocks, changes in their properties or a stress-strain state. Additionally, Paudel *et al.* (2018) and Spivak *et al.* (2019) found changes in the chemical composition and/or ground water temperature. Arai *et al.* (2011) studied AP changes caused by the earthquake off the Western Pacific coast of Tohoku (M_w9.0) in Japan in 2011, identified by means of atmospheric boundary waves excited by the rising and falling surface of the ocean, based on the waveform characteristics and the similarity with the data from water bottom pressure tide gauges.

Dragani *et al.* (2009) studied the vulnerability of the coastlines in the southernmost tip of South America and Antarctica to potential tectonic tsunamis (caused by undersea earthquakes) with epicenters in the region of the Scotia Arc (Orcadas, Georgias del Sur, Sandwich del Sur and Elephant islands). For example, on August 4, 2003, an M_w 7.6 earthquake, whose epicenter was located 71 km ENE of the Orcadas del Sur Islands, in Antarctica, caused a tsunami that was mitigated by the presence of 2 m-thick sea ice surrounding the islands (Roucco and del Valle, 2021). Dragani *et al.* (2009) concluded that, even though the Patagonian coastline shows a relatively low vulnerability to these phenomena, it is necessary to conduct a comprehensive study assessing the potential impact of tsunamis due to the high rate of occurrence of violent geological processes in the Scotia Arc. The joint action of a tsunami, even of a low magnitude, the local tide and the storm surge may aggravate the situation, especially in the case of low areas located a few meters above sea level. Based on observations and numerical modeling, many authors (among them, Ayca and Lynett, 2016; Kowalik and Proshutinsky, 2010; Lee *et al.*, 2015; Shelby *et al.*, 2016) demonstrated that the reach of a tsunami in rivers, coves and estuaries is strongly affected by tidal conditions. Another major factor to be considered is that tsunamis result in periodical oscillations caused by the geometrical features of the area, such as seiches (Rabinovich, 2010). The areas of Puerto Argentino, on the Malvinas Islands, and Mar del Plata and Quequén, in the province of Buenos Aires, promote the formation of seiches. Woodworth *et al.* (2005) detected in Puerto Argentino two continuous energy peaks with 87 and 26 min periods, identified as seiches.

On August 12, 2021 the region was shaken by an M_w7.5 earthquake that was 47 km deep, and three minutes later, by another M_w8.1 earthquake, which was 56 km deep and 90 km away from the previous one. Even though the surge was not destructive, it was the first one since the catastrophic tsunami in 2004, which hit three different oceans (Jia *et al.*, 2022).

This study selected $M_w \geq 6.6$ earthquakes since 1970. The time series of available GMF activity data, sunspot

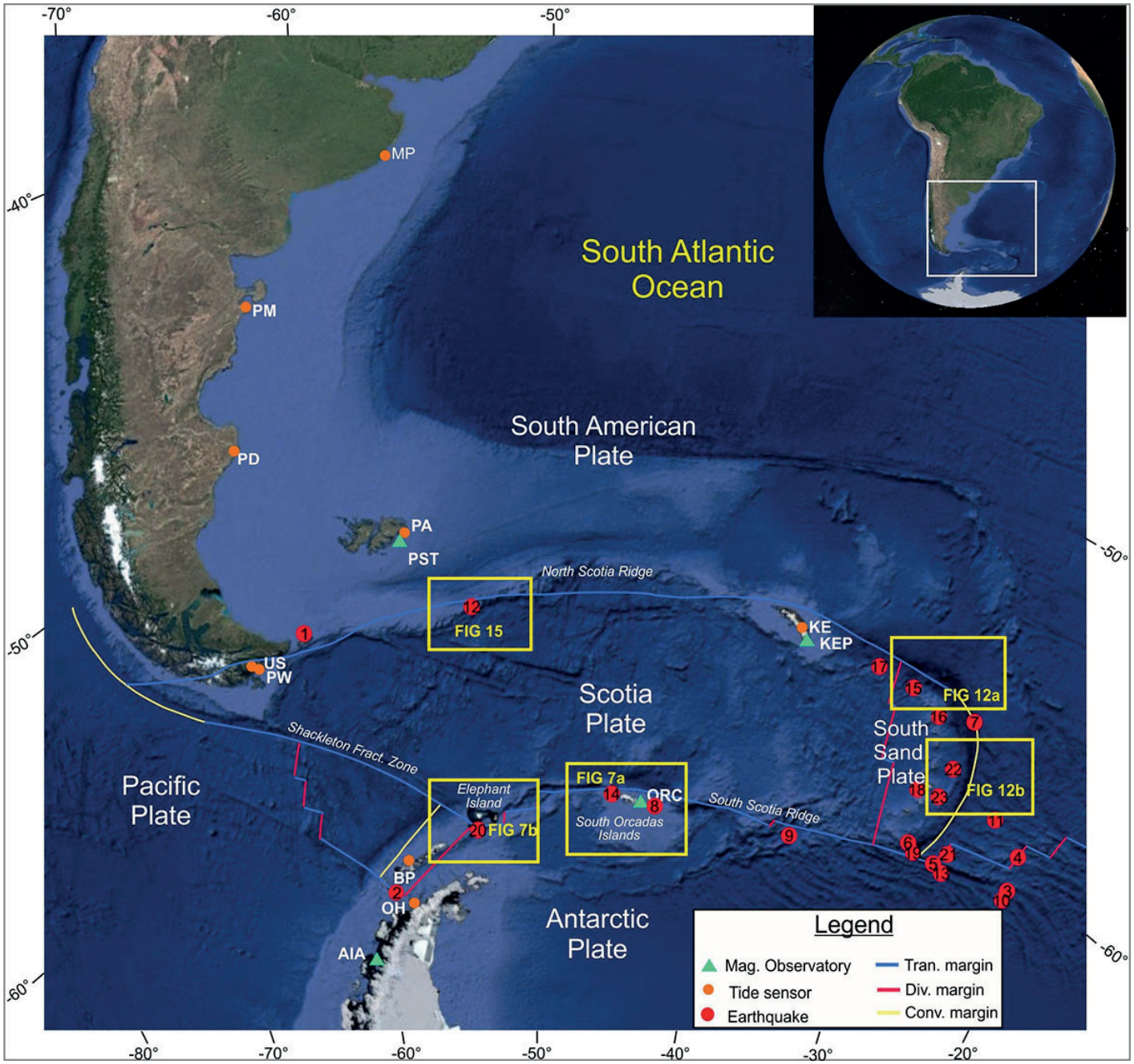

Figure 1. Location of Mw≥6.6 earthquakes in the last 20 years in the South Atlantic. Earthquakes (red circles) numbering of earthquakes in Table 1.. Margins of the South American, Scotia, South Sandwich and Antarctic pates (blue line: transcurrent margin; red line: divergent margin; and yellow line: convergent margin). Geomagnetic observatories (green triangles): Puerto Argentino (PST), King Edward Point (KEP), Argentine Island - Antarctica (AIA), Orcadas Islands (ORC). Tide stations (orange dots): King Edward (KE), Puerto Argentino (PA), Base Prat (BP), O'Higgins (OH), Puerto Williams (PW), Ushuaia (US), Puerto Deseado (PD), Puerto Madryn (PM) and Mar del Plata (MP). (Background photo taken from **http://ds.iris.edu/**)

number, WL from tide stations and AP at ocean level were analyzed. These studies were conducted based on: a) the GMF harmonic analysis applying the wavelet method and frequency filters, b) the analysis of WL residues, obtained after eliminating the astronomical tide effect, and c) the observation of the discrepancies between AP hourly grids and the analysis of the AP time series variation in three to four hours periods.

This study aims at improving the knowledge of the magnetic field, WL and AP in the presence of earthquakes in the area of the Scotia Sea. In addition, maximum heights following significant seismic events in the western coastal regions of the South Atlantic and Antarctica were analyzed as these regions can be reached by potential earthquake-generated tsunamis.

Area Under Study

The Scotia plate is located south of the South American plate, mainly in the South Atlantic Ocean, between parallels 53° S and 63° S and between meridians 25° W and 70° W, formed by oceanic lithosphere and small continental crust fragments of the Georgias del Sur and Orcadas del Sur Islands. Its boundaries are represented by the Shackleton Fracture Zone to the west and a large part of the Scotia Arc to the north, east and south. The north of the Scotia plate is represented by a transcurrent-type margin that goes through southern Tierra del Fuego up to the Georgias del Sur Islands. To the east, this pate has a divergent and also active margin, which separates it from the South Sandwich microplate, and to the south, a mixed margin (divergent and mostly transcurrent) that is represented by the South Scotia Ridge (Figure 1).

The South Sandwich microplate is located east of the Scotia Sea, between coordinates 55° S and 60° S, and it is bounded on the north and east by the South American plate, on the south by the Antarctic plate, and on the west by the Scotia plate. The Sandwich del Sur Islands and their associated seamounts make up the volcanic arc of a highly active subduction system located in the South Atlantic (South Sandwich arc) (Eagles, 2010; Leat *et al.*, 2013, 2016; Dalziel *et al.*, 2013; Maldonado *et al.*, 2013, 2015) (Figure 1).

The subduction area of the South American plate beneath the South Sandwich plate is one of the regions with the highest seismic activity in the planet (Beniest and Schellart, 2020; Larocca *et al.*, 2019; 2021). In addition, it is one of the regions in the Atlantic Ocean with a great potential to generate tsunamis due to its seismic and volcanic activity (Dragani *et al.*, 2006; 2009). These authors detected sea level oscillations in the order of 20 cm on the shores of the province of Buenos Aires caused by the M_w9.3 earthquake that hit the western coastline of northern Sumatra over 15,000 km away on December 26, 2004.

Since 1970, in this area there have been more than 20 M_w>6.6 seismic events, of which over a half have exceeded a magnitude of M_w7 (Table 1). The largest in this series, reaching M_w8.1, occurred on August 12, 2021 south of the region of the Sandwich del Sur Islands, and the following one in intensity reached M_w7.7, on November 17, 2013, in the vicinity of Laurie Island, where the permanent Argentine Antarctic base Orcadas is located (Figure 1).

Table 1. Seismic events of Mw>6.6 from 1970 to 2021. Date, magnitude and location. Information from the USGS and INPRES.

N°	Year	Month	Day	TIME (UT)	Latitude (°)	Longitude (°)	Depth (km)	Mag (MW)	Region
1	1970	6	15	11:14:51	-54.476	-64.499	10	7.2	Tierra del Fuego, Argentina region
2	1971	2	8	21:04:20	-63.398	-61.377	13	7	South Shetland Islands
3	1973	10	6	15:07:37	-60.823	-21.549	33	7	East of the South Sandwich Islands
4	1977	8	26	19:50:01	-59.426	-20.508	33	7.1	East of the South Sandwich Islands
5	1983	10	22	04:21:35	-60.665	-25.451	24	7.2	South Sandwich Islands region
6	1987	1	30	22:29:42	-60.063	-26.916	48	7	South Sandwich Islands region
7	1991	12	27	04:05:58	-56.032	-25.266	10	7.2	South Sandwich Islands region
8	2003	8	4	04:37:20	-60.532	-43.411	10	7.6	Scotia Sea
9	2006	8	20	03:41:48	-61.029	-34.371	13	7	Scotia Sea
10	2006	1	2	06:10:49	-60.957	-21.606	13	7.4	East of the South Sandwich Islands
11	2008	6	30	06:17:43	-58.227	-22.099	8	7	South Sandwich Islands region
12	2013	11	25	06:27:33	-53.9451	-55.0033	12	7	Malvinas Islands region
13	2013	7	15	14:03:39	-60.857	-25.07	11	7.3	218 km SSE of Bristol Island, South Sandwich Islands
14	2013	11	17	09:04:55	-60.2738	-46.4011	10	7.7	Scotia Sea
15	2014	6	29	07:52:50	-55.4703	-28.3956	8	6.9	154 km NNW of Visokoi Island
16	2016	5	28	09:46:59	-56.2409	-26.9353	78	7.2	53 km NNE of Visokoi Island, South Sandwich Islands
17	2016	8	19	07:32:22	-55.2852	-31.8766	10	7.4	South Georgia Island region
18	2018	12	11	02:26:29	-58.5446	-26.3856	133	7.1	54 km N of Bristol Island, South Sandwich Islands
19	2019	8	27	23:55:19	-60.2152	-26.5801	12	6.6	131 km S of Bristol Island, South Sandwich Islands
20	2021	1	23	23:36:50	-61.8117	-55.4903	10	6.9	South Shetland Islands
21	2021	8	22	21:33:20	-60.2897	-24.8801	14	7.1	South Sandwich Islands region
22	2021	8	12	18:32:52	-57.5674	-25.0316	47	7.5	South Sandwich Islands region
23	2021	8	12	18:35:20	-58.4513	-25.327	56	8.1	South Sandwich Islands region

The water level observed at a tide station results from the combination of the mean level, astronomical tide, storm surge and, on some occasions, additional effects, such as seiches, meteotsunamis and tsunamis. The simultaneous action of these factors or some of them is rare. Nevertheless, there are more susceptible regions where values that are not extreme may affect the shores, causing flash flooding.

The astronomical tide amplitudes in the continental shelf of the Southwestern Atlantic are some of the greatest in the world, reaching 12 m south of the province of Santa Cruz and falling to 5.45 m in Puerto Deseado, 3.91 m in Puerto Madryn, and 1.74 m in Mar del Plata (Argentine Naval Hydrographic Service, 2022). The storm surge amplitude also varies considerably in the area under study. The maximum values of these phenomena are usually below 0.50 m at King Edward Point, Base Prat and O'Higgins, and below 0.80 m at Puerto Williams, Ushuaia and Puerto Argentino. In addition, storm surges are not usually above 1.30 m in Puerto Deseado or Mar del Plata, or 1.5 m in Puerto Madryn. The various combinations of tides and storm surges, together with other phenomena in the area under study, may lead a potential tsunami spreading in the area, even one with small amplitude, to have a significant effect on one region, but not on another. Thus, it is necessary to analyze sea levels at the different tide stations.

Data

This study compiled GMF data from observatories of the International Real-time Magnetic Observatory Network (INTERMAGNET), AP data at sea level from the Global Modeling and Assimilation Office (GMAO) published in the database MERRA-2 (Rienecker *et al.*, 2021), WL records from tide stations of the Intergovernmental Oceanographic Commission (IOC) (Flanders Marine Institute, 2021) and information about $M_w > 6.6$ earthquakes from the United States Geological Service (USGS) and the Argentine Institute of Seismic Forecasting (INPRES) in the area under study of the South Atlantic on the earthquake occurrence dates in Universal Time (UT).

The observatories selected from the INTERMAGNET network in the area were King Edward Point (KEP) (54.3° S; 36.5° W), Puerto Argentino/Port Stanley (PST) (51.7° S; 57.8° W), Orcadas Islands (ORC) (60.7° S; 44.7° W) and Faraday Islands Argentine Island- Akademik Vernadsky Base (AIA) (65.25° S; 64.25° W), whose data are available at **https://intermagnet.github.io**. These observatories provide information about GMF components per minute. The observatories report the components of the horizontal plane (X and Y) and the vertical axis (Z), as well as Declination (D) and Horizontal component (H). The INTERMAGNET network has GMF data in the area since 2003, that is why, from that year, 16 $M_w > 6.6$ seismic events were chosen.

In addition, geomagnetic activities indices Dst (Disturbance Storm Time) and AE (Auroral Electrojet) were considered for the purposes of disregarding observations due to rapid geomagnetic variations caused by solar activity. Dst monitors magnetic variations due to an increased ring current, measured in nT. AE represents the global activity of electrojets in the auroral zone, measured in nT (Davis and Sugiura, 1966). These indices are available at the World Data Center for Geomagnetism, Kyoto (WDC for Geomag.) (**http://wdc.kugi.kyoto-u.ac.jp/wdc/Sec3.html)**.

In addition, so as to compare the solar activity cycles with the biggest earthquakes in the 1970s, the analysis included the sunspot number, available at WDC-SILSO, Royal Observatory of Belgium, Brussels (**http://www.sidc.be/SILSO/)**.

Table 2. Stations with available WL data on the earthquake date, and type of sensor recording the data (Pressure: P; Radar: R; Floating: F; Acoustic: A).

Date	Depth (km)	Mag (Mw)	KE	PA	BP	OH	PW	US	PD	PM	MP
2003/08/04	8	7	-	R	-	-	P	-	-	-	-
2013/07/15	11	7.3	P	R	P	-	P	-	-	P	F
2013/11/17	10	7.7	P	R	P	-	P	-	F	P	R
2013/11/25	11.8	7	P	R	P	-	P	-	F	P	R
2016/05/28	78	7.2	P	P	P	-	P	R	F	P	R
2016/08/19	10	7.4	P	P	P	-	P	R	F	P	R
2018/12/11	133	7.1	P	-	P	-	P	R	F	P	F
2021/08/12	47	7.5	P	P	P	P	P	R	F	P	F
2021/08/12	55.7	8.1	P	P	P	P	P	R	F	P	F
2021/08/12	47.2	7.5	P	P	P	P	P	R	F	P	F
2021/08/22	14	7.1	P	P	P	P	P	R	F	P	F

WL information was obtained from tide stations King Edward (KE) (54.28° S; 36.5° W), Puerto Argentino (PA) (51.75° S; 57.93° W), Base Prat (BP) (62.48° S; 59.66° W), O'Higgins (OH) (63.32° S; 57.90° W), Puerto Williams (PW) (54.93° S; 67.61° W), Ushuaia (US) (54.82° S; 68.22° W), Puerto Deseado (PD) (47.75° S; 65.91° W), Puerto Madryn (PM) (42.76° S; 65.03° W) and Mar del Plata (MP) (38.00° S; 57.54° W), shown on Figure 1, provided by the Sea Level Station Monitoring Facility (**https://www.ioc-sealevelmonitoring.org/**). These observatories provide information about WL per minute. Table 2 shows the stations with available WL records and the sensor used.

Sea-level AP in grids and time series from global data (Rienecker *et al.*, 2021) are obtained from the MERRA-2 database (Modern-Era Retrospective analysis for Research and Applications, Version 2) of NASA's Global Modeling and Assimilation Office (GMAO). This database draws on models of multiple data sets using a fixed assimilation system, and provides data about atmosphere, earth and ocean conditions since 1980, with a spatial resolution of 0.5° × 0.667° (approximately 50 km × 50 km) and a time resolution of 1 hour (**https://gmao.gsfc.nasa.gov/reanalysis/MERRA-2/**)

The characteristics of the earthquakes, such as date, time, magnitude, location, and depth, among others, are available at USGS (**https://earthquake.usgs.gov/earthquakes/**) and INPRES (**https://www.inpres.gob.ar/**) (Table 1).

Methodology

Treatment of the magnetic field data

With the aim of finding patterns in the behavior of the solar magnetic activity and the detection of $M_w \geq 6.6$ earthquakes, the smoothed curve of the daily sunspot number average of the solar cycles between 1970 and 2021, from the end of cycle 20 to the beginning of 25, was contrasted to the occurrence of seismic events (Figure 2).

To obtain the GMF component without secular variation, the GMF horizontal component from the International Geomagnetic Reference Frame (IGRF), **https://www.ngdc.noaa.gov/geomag/**), calculated based on the date and location of each observatory, was subtracted, as per (1).

$$H_{OBS.} = H_{OBS.INTER} - H_{IGRF} \quad (1)$$

where:

H_{OBS} is the GMF horizontal component of the Observatory without secular variation.

$H_{OBS.INTER}$ is the GMF horizontal component measured at each observatory from the INTERMAGNET network.

H_{IGRF} is the GMF horizontal component corresponding to the IGRF.

In addition, the data from observatories, taken in pairs, were deducted from each other, considering the proximity of the earthquake to the network observatory so that the farthest observatory could play the role of a Base Station (H_{Base}) and the closest one that of a field observation point ($H_{Closest}$) according to Larocca *et al.* (2021). Therefore, the differences calculated, referred to as deltas (ΔH), minimized the solar diurnal variation effects, as per (2).

$$\Delta H = H_{Base} - H_{Closest} \quad (2)$$

where: ΔH is the GMF without diurnal variation.

H_{Base} is the GMF horizontal component of the farthest observatory.

$H_{Closest}$ is the GMF horizontal component of the closest observatory.

As the time series of geomagnetic data are non-seasonal and linear, it is appropriate to perform the analysis with adequate methods, such as the continuous wavelet transform (CWT), which, within the mathematical field of harmonic analysis, provides an optimum resolution in the time-frequency plane, thus allowing for an excellent characterization of the series (Grinsted *et al.*, 2004). To this effect, the CWT was applied to the ΔH of the magnetic field at observatories, using the Morlet wavelet (con $\omega_0 = 6$) because it provides an adequate balance between time and frequency location. In addition, the solar activity was assessed based on the hourly values of the Dst and AE indices so as to identify geomagnetic storms (Gulyaeva, 2014) on the earthquake occurrence date as they can mask ΔH.

Moreover, a high-pass filter (*HPF*) with a cut-off frequency of 4 mHz was applied to the ΔH, up to 5 hours before and after the earthquake, for the purposes of identifying anomalous frequencies before the earthquake in the GMF, thus yielding the *F* ΔH.

Treatment of sea-level AP variation levels

For the purposes of detecting AP behavior patterns around a seismic event, the time evolution of the sea-level pressure was calculated, taking the mean value of pixels around the earthquake epicenter. Arai *et al.* (2011) observed that, around the earthquake detection time, the pressure drops and subsequently increases rapidly.

A space-time analysis was conducted in the area to study the sea-level AP behavior. Data were downloaded into a 4º×4º grid one or two hours before and after the earthquake. As the MERRA-2 database provides hourly information, the closest hour was rounded off. For each event, two raster-format grids were obtained. The difference between both grids was calculated, subtracting AP data before and after the earthquake. Table 3 shows the period and magnitude of this variation for each event analyzed.

Table 3. Details of the date and time of the earthquakes studied, before and after time from the MERRA-2 database grid and difference in atmospheric pressure at the location of each earthquake.

Date and time of the earthquake	Time of AP_1 (before the earthquake) (UT)	Time of AP_2 (post-earthquake) (UT)	Atmospheric pressure difference $\Delta AP = AP_2 - AP_1$ [hPa]
2003/08/04; 4:37	4:00	5:00	3.40
2006/01/02; 6:10	5:00	7:00	-0.58
2006/08/20; 3:41	2:00	4:00	-0.20
2008/06/30; 6:17	5:00	7:00	3.48
2013/07/15; 14:03	13:00	15:00	-1.80
2013/11/17; 9:04	8:00	10:00	1.65
2013/11/25; 6:27	6:00	7:00	1.04
2014/06/29; 7:52	7:00	9:00	0.65
2016/05/28; 9:46	9:00	11:00	1.77
2016/08/19; 7:32	6:00	9:00	0.85
2018/12/11; 2:26	2:00	3:00	-0.75
2019/08/27; 23:55	23:00	2:00	1.36
2021/01/23; 23:36	23:00	24:00	-0.013
2021/08/12; 18:32	18:00	19:00	-0.02
2021/08/12; 18:36	18:00	19:00	-0.3
2021/08/22; 21:33	21:00	20:02	0.7

Treatment of WL data

WL information from available sensors was downloaded for each event, and their quality was controlled using the methodology applied for the network of tide stations of the Argentine Naval Hydrographic Service (Banegas *et al.* 2021). Harmonic analyses were performed following the methodology applied by Oreiro *et al.* (2014) for the sites where harmonic constants were not available (BP, BW, OH, KP) using series with, at least, 2-year observations. Only waves with amplitudes over 5 mm were selected. For all stations, astronomical tide predictions were made 10 days before and 10 days after the moment when each earthquake occurred. The levels observed were subtracted from the predictions, yielding the residue, which was subsequently plotted for each event, for all the stations available. Then, it was sought to identify the effect of the tsunami on each station, so as to keep track of the signal, and maximum amplitudes associated with the event were analyzed.

Results

Overlapping the curve of the monthly sunspot number with the occurrence of large magnitude earthquakes from 1970 to 2021 allowed for the identification of a greater number of earthquakes during solar cycle 24 (SC24), approximately between 2010 and 2020. In addition, 65% of the seismic events occurred in periods when the monthly sunspot number was below 100 spots. Also, of a total of 23 earthquakes (Table 1), it was confirmed that 16 occurred in periods of decreased solar activity, while only 7 occurred in increased activity periods. Moreover, only 5 earthquakes coincide with the maximums of the cycles, and 2, with the minimums (Figure 2).

The Scotia and South Sandwich plates have margins of various types with distinguishing tectonic features; however, all of them show great seismic activity. Therefore, this paper was organized presenting studies according to their relative position with respect to the boundaries of the Scotia and Sandwich plates. The GMF, WL and AP results were grouped into three titles for the South Scotia ridge, the South Sandwich Arc and the North Scotia Ridge areas.

South Scotia Ridge

The events on November 17, 2013 (M_w 7.7) and January 23, 2021 (M_w6.9) were selected as representative of the study of the area based on the analysis of GMF variations and geomagnetic activity indices in an interval of ±5 hours from the occurrence of earthquakes.

The continuous wavelet transform for the ΔH observed between the different observatories was performed (Figure 3). The thick black contour lines show a 5% significance level against the red noise background, and the cone of influence (COI) shows the edge effects on the image, which are blurry.

The WT power spectra on the ΔH component from the observatories chosen (Figure 3a and b) during a period of ± 5 hours, centered on the selected earthquake, show high-energy areas in periods of 0.05 h to 0.25 h, between 1 and 3 hours before its occurrence. The spectral analysis

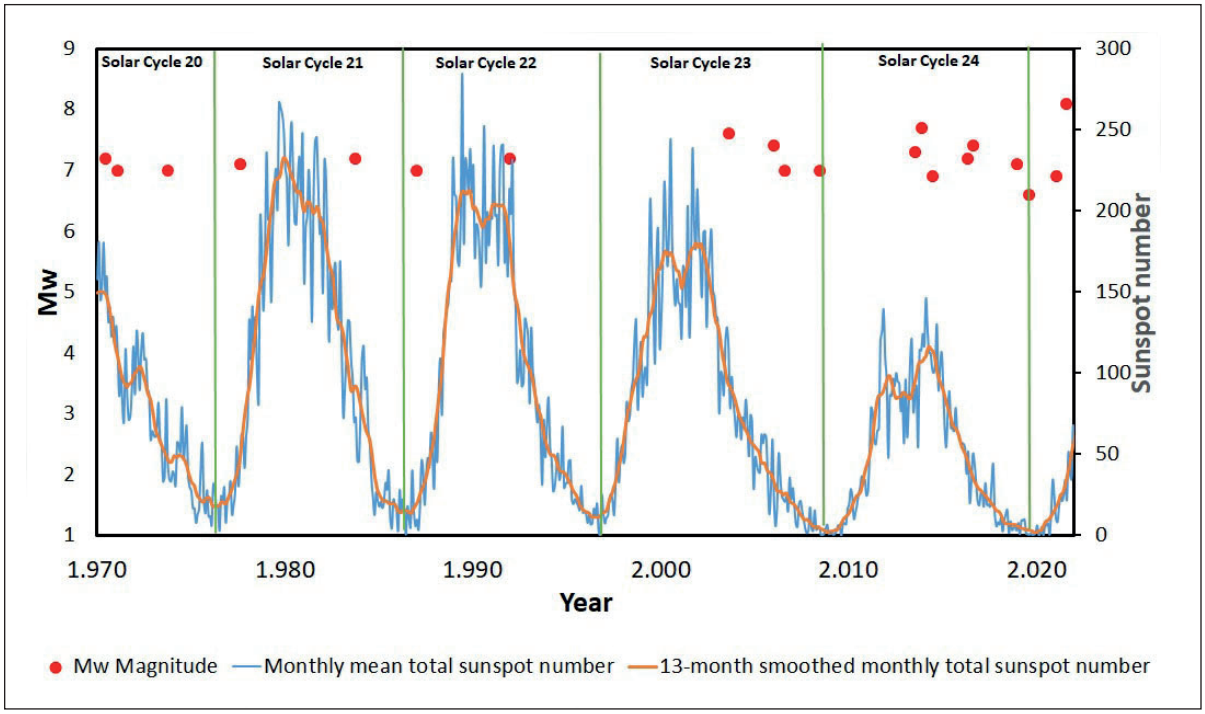

Figure 2. Graph with solar cycles and occurrence of large-magnitude seismic events since the 1970s. Monthly sunspot number (blue line) and smoothed sunspot number (red line). Start/end of solar cycles (SC) 21-25 (vertical grey lines). Earthquakes (red dots).

of the earthquake on November 17, 2013 shows a 2-4 Hz high-energy area (areas surrounded by black lines) in periods between 0.125 and 0.25 h, one hour after the event, in the presence of a solar activity index Dst of -25 nT, suggesting a weak magnetic storm, as confirmed by the AE index value above 280 nT (Figure 3 a).

While the earthquake on January 23, 2021 showed high-energy areas from the moment of the earthquake to 2 hours before and 1 hour after it, covering the entire frequency spectrum 2 hours before its occurrence, on that day the Dst index did not show geomagnetic storms (Figure 3b).

The effect of covering a wide range of frequencies around the earthquake with high energies is repeated before and after the events on August 4, 2003 and August 20, 2006, also located in the area under study, with similar magnitudes and depths.

A cross wavelet correlation (XWT) between the most intense earthquakes (August 4, 2003-November 17, 2013) with M_w7.6 and 7.0, respectively, and the least intense ones (August 20, 2006-January 23, 2021) with M_w7.0 and 6.9, respectively, was calculated separately (Figure 4a and b). The figures were drawn centered on the moment when each earthquake occurred for the purposes of highlighting common frequencies before and after both earthquakes. Both correlations show that 2-hour high-energy periods coincide up to 3 hours before and after the events. In addition, between 1 and 3 hours before and after the zero hour, direct and inverse correlations can be found (Figure 4a and b).

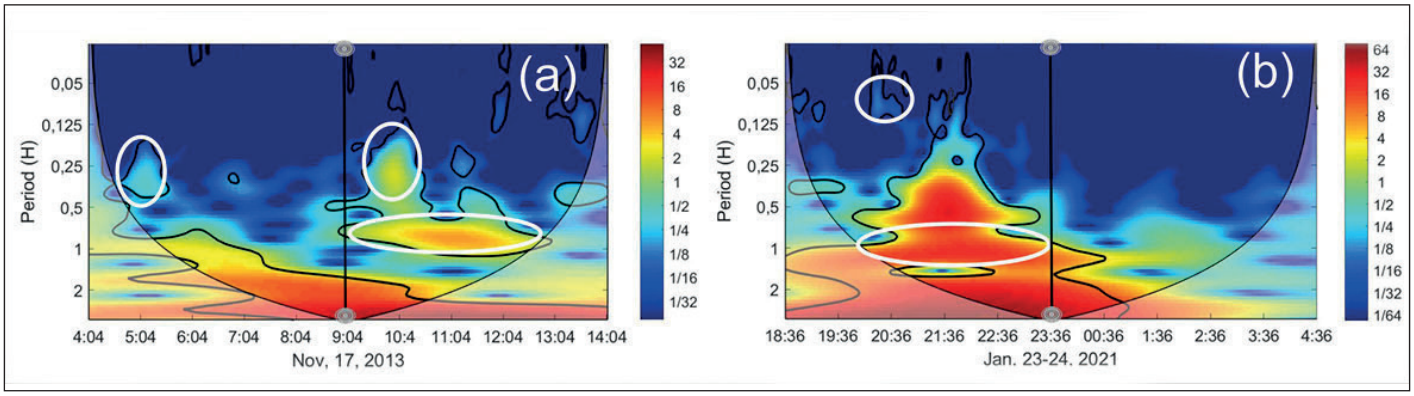

Figure 3. Continuous wavelet transform of ΔH, centered on the moment when the earthquake occurred, with a ± 5 hour range; (a) ΔAIA-ORC: November 17, 2013; (b) ΔAIA-PST: January 23-24, 2021. Earthquake (gray bar).

An HPF with a cutoff wavelength of 4 min was applied to the ΔH among observatories AIA, PST and KEP. The filtering shows oscillations with an amplitude between ±0.5 and 2 nT, occurring between 2 and 6 hours before the event (Figure 5a and b). The filtering of the seismic event on November 17, 2013 shows a significant amplitude for around 7 minutes (Figure 5a), while the event on January 21, 2021 shows the same significant amplitude for 40 minutes (Figure 5a). In both cases, events were preceded by a series of earthquakes (M_w 5.8 to 4.4) for the same length of time.

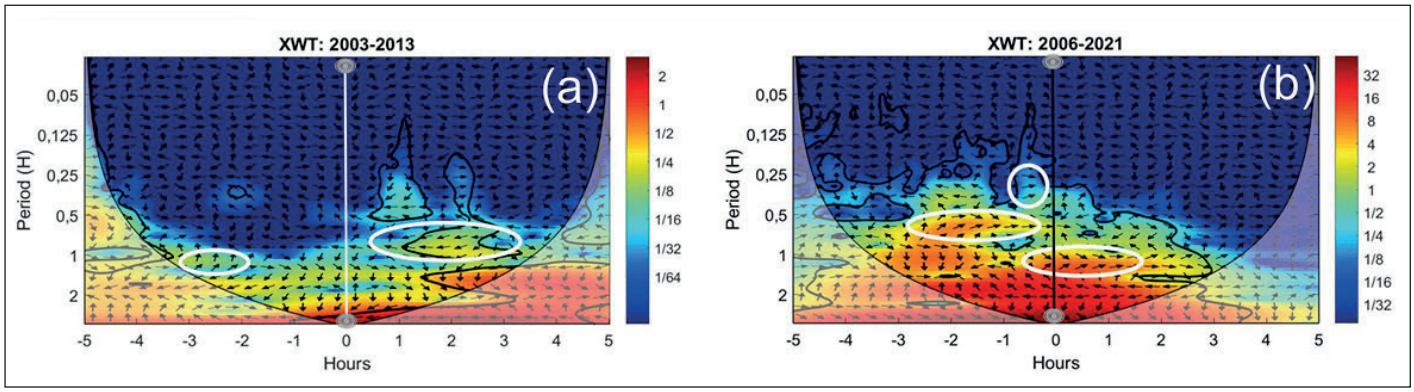

Figure 4. Crossed wavelet correlation (XWT) centered on the earthquake, between events on August 4, 2003 and November 17, 2013 (a); between events on August 20, 2006 and January 23, 2021 (b). High significance level (black curves). Direct and inverse correlation (white ovals). COI edge effects (blurry image).

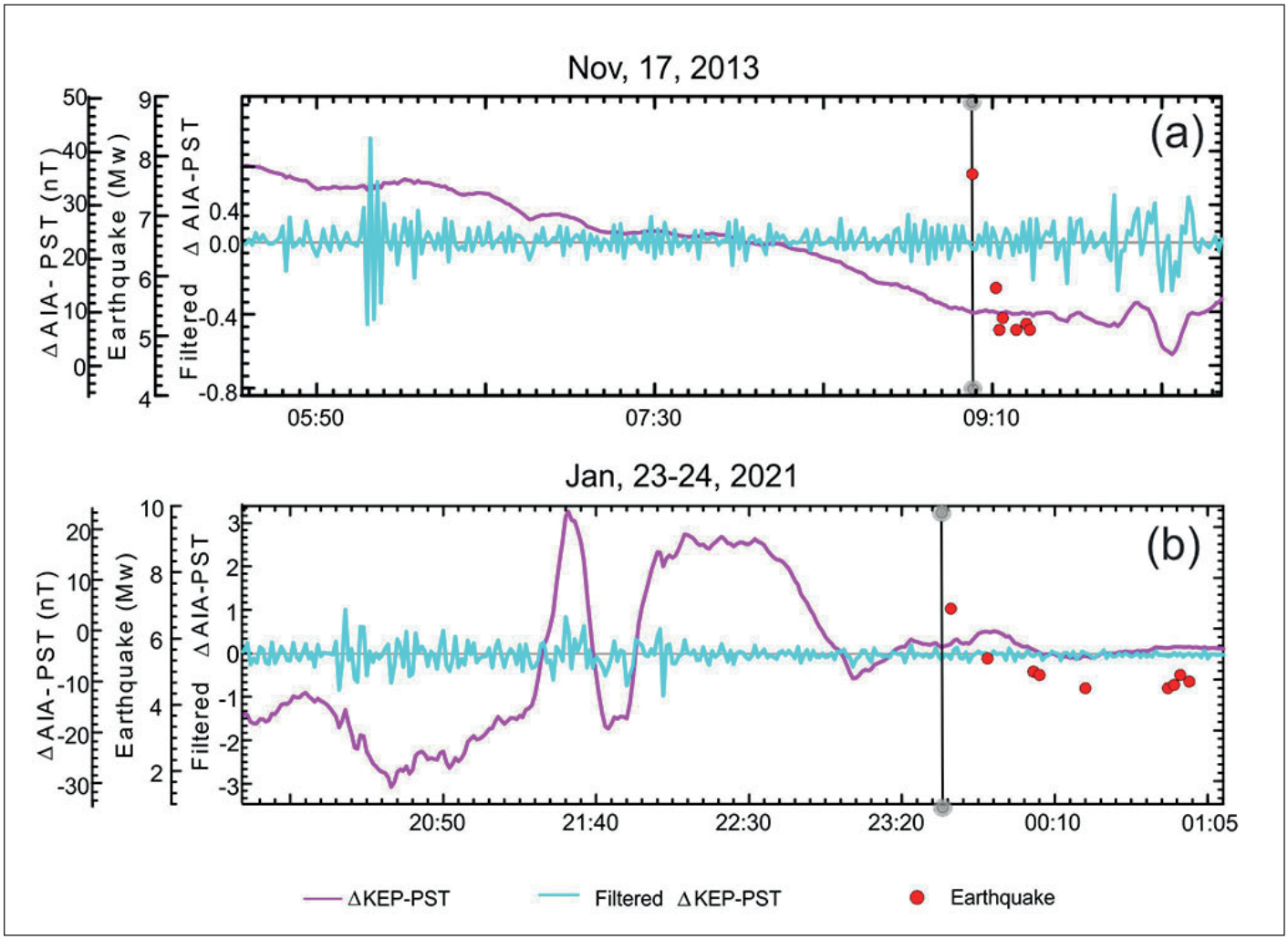

Figure 5. Difference of the H component of the magnetic field between observatories (ΔH) (magenta line). Filtered ΔH (cyan line). Earthquake (red dot). (a) ΔAIA-PST Nov 17, 2013; (b) ΔAIA-PST Jan 23, 2021.

Figure 6 shows the WL measured by the available tide stations on November 17, 2003, when the earthquake occurred (M_w7.7), and 4 days after the event; this is the only $M_w \geq 7$ magnitude event occurring in the area and for which there is available WL information. A disturbance that may be associated with the earthquake is shown, around 2.5 hours after the occurrence of the event at KE, ~930 km away, and a mild disturbance at PD, PM and MP, more than 12 hours later (Figure 6). In all cases, the disturbances show amplitudes in the order of 0.30 m, not posing potential risks, even if combined with storm surge events, like at PM and MP.

Figure 7 shows the results of the space-time analysis of the sea-level pressure variation in this area. For the earthquake on November 17, 2003, between 8:00 and 10:00 (UTC) (Table 3), around the earthquake epicenter (gray bar), an area of disturbance can be seen in the isobars, as well as pressure variation in the time series (Figure 7a and c). The AP difference represented by isobars shows a force field parallel to the transcurrent margin where the tighter lines would suggest greater stress. It is worth pointing out that 7 minutes later, an M_w5.8 earthquake occurred 200 km away from the previous one, aligned parallel to the transcurrent margin, which is why it is associated with the disturbance of isobar lines.

In addition, analyzing the earthquake on January 23, 2021 between 23:00 and 24:00 (UTC) (Table 3), we can see that within one hour from the moment when the event chosen occurred, 7 earthquakes more with magnitudes between M_w5.4 and M_w4.6 are detected. They are distributed in the area forming a wedge, not more than 30 km away from the earthquake under study, following the same pattern as that of isobars, as shown on Figure 7b. Figure 7d shows that the AP maximum occurs in the same time span. After the main earthquake, the AP drops to 0.3 hPa.

South Sandwich Arc

The most representative earthquakes in this area, occurring on June 29, 2014 (M_w6.9) and August 12, 2021 (M_w7.5 and 8.1) were analyzed. Rapid GMF variations and geomagnetic activity indices were studied in an interval of ± 5 hours from the occurrence of the earthquakes.

In addition, the continuous wavelet transform for the ΔH found among observatories KEP, PST and ORC was applied (Figure 8). It is observed that, in the time range centered on the earthquake, there are high-energy areas in periods between 0.125 and 0.50 hours, between 2 and 4 hours before or after the earthquake on June 29, 2014 (M_w6.9) at a depth of only 8 km (Figure 8a).

Meanwhile, Figure 8b shows bunch-like high frequency ranges before and after the events, given that two highly intense earthquakes (M_w7.5 and 8.1) occurred at a great depth (47 and 56 km), separated by 3 minutes and only 90 km away, which does not allow for a clear definition in a frequency range, and, within one hour, more than 5 earthquakes with intensities in the order of M_w5.9 are also added.

A cross correlation between the earthquakes (June 29, 2014-August 12, 2021) was calculated (Figure 9). The figure was drawn centering each earthquake (0 hour) for the purposes of highlighting common frequencies before and after both earthquakes. No areas of high energy significance are shown, probably due to the fact that the correlated earthquakes occurred at very different depths. In spite of that,

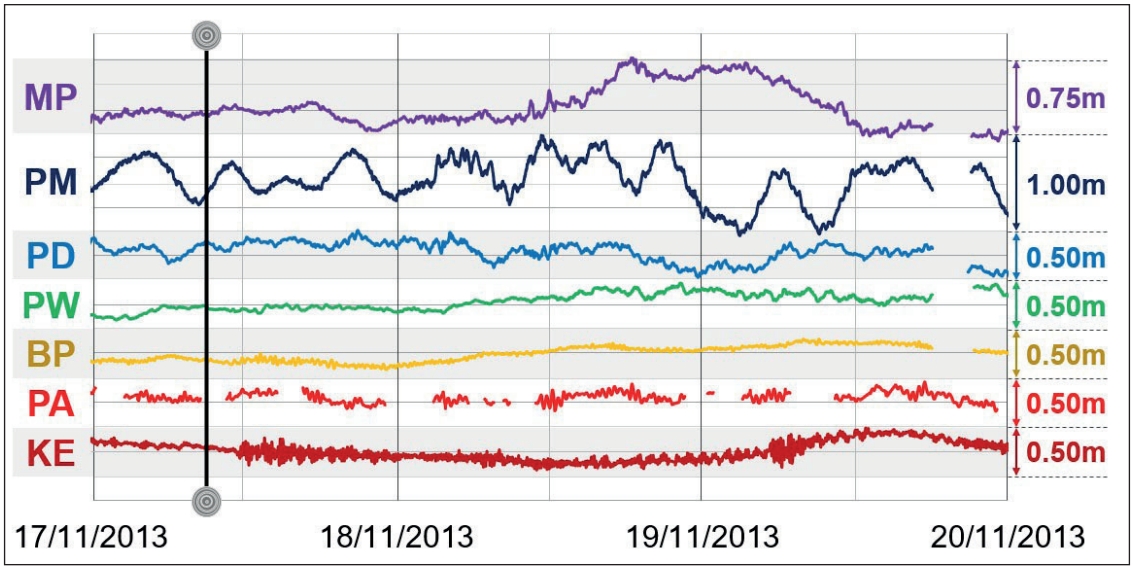

Figure 6. WL measurement from tide stations King Edward (KE), Puerto Argentino (PA), Base Prat (BP), O'Higgins (OH), Puerto Williams (PW), Ushuaia (US), Puerto Deseado (PD), Puerto Madryn (PM) and Mar del Plata (MP), after the earthquake on November 17, 2003 (M_w7.7) at 9:04 (UTC), at a depth of 11.8 km (black vertical line).

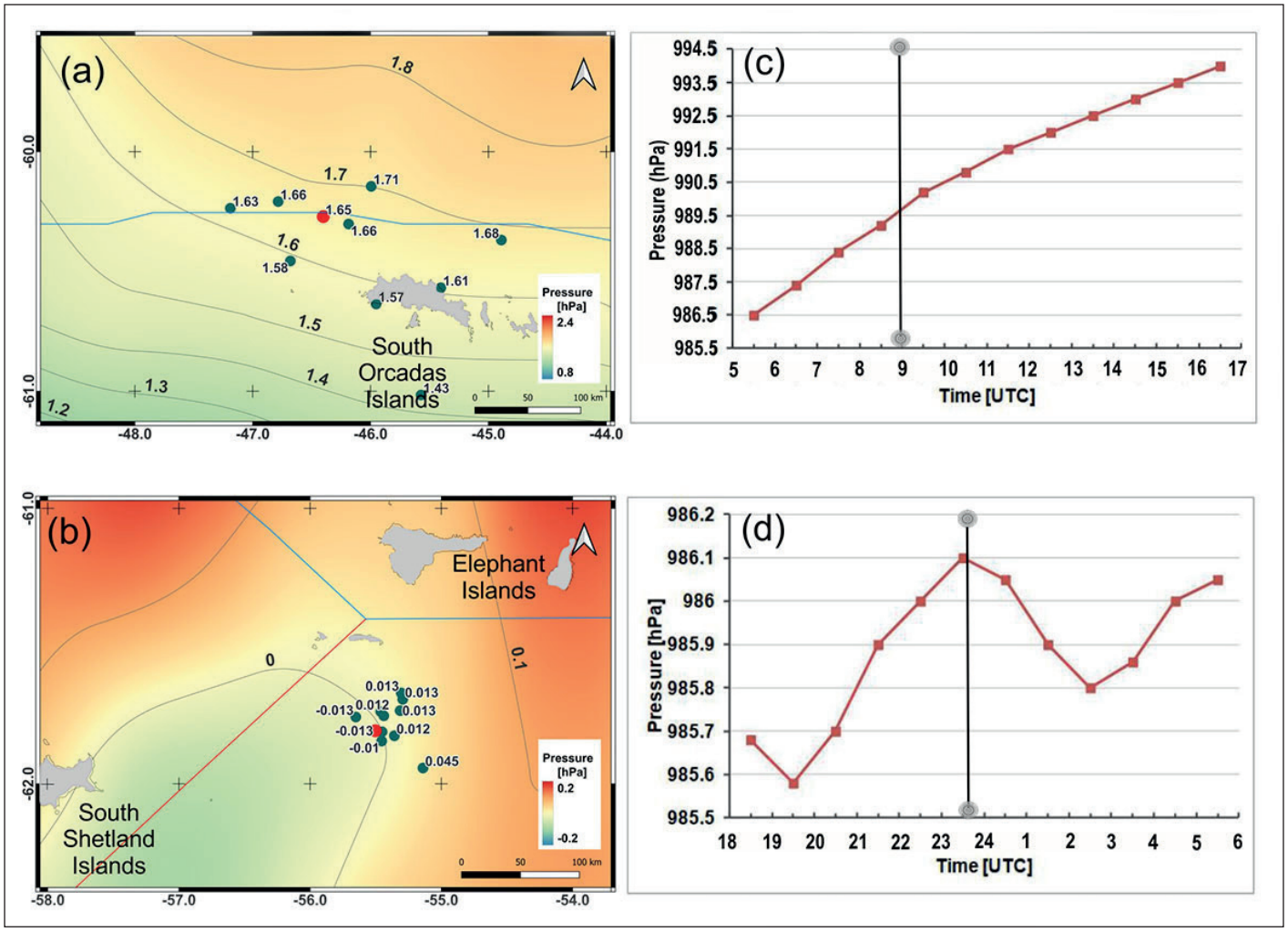

Figure 7. Differences of ocean-level AP grids on: (a) Nov 17, 2013, (8:00 -10:00); (b) Jan 23, 2021, (23:00-24:00). Time series of sea-level hourly AP: (c) Nov 17, 2013 (5:30 - 16:30); (d) Jan 23-24, 2021 (18:30 - 5:30). Plate margins: divergent margin (red line); transcurrent margin (blue line). Earthquakes: position according to the coordinates of their epicenter (left) (red dots). Local difference (green dots); time location (right) (gray bar).

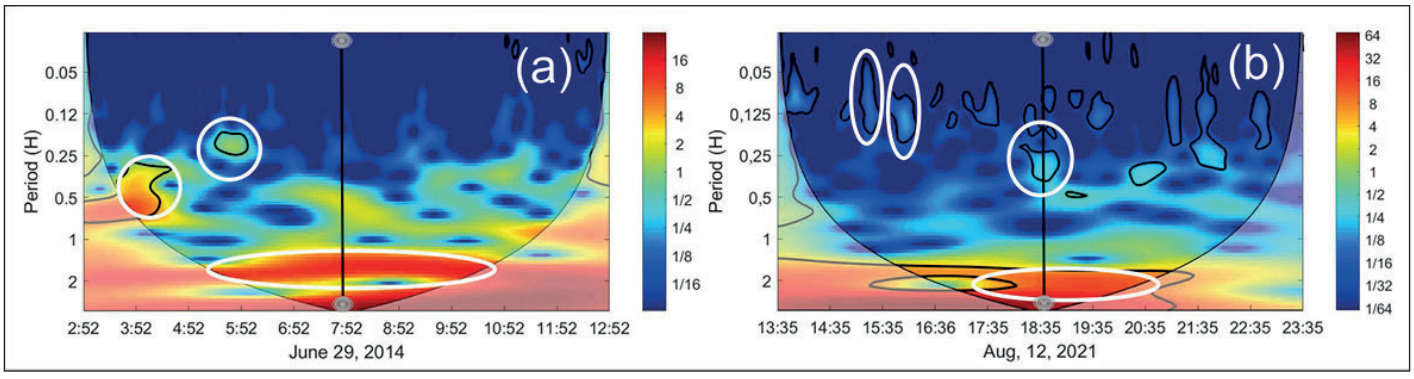

Figure 8. Continuous wavelet transform ΔH, centered on the moment when the earthquake occurred, with a ± 5 hours range; (a) ΔKEP-ORC: June 29, 2014; (b) ΔKEP- PST: August 12, 2021. Earthquake (black bar).

in an interval between 1 and 2 hours before the events, a certain correlation for a period of 1 to 2 hours (medium to high frequencies) can be seen.

An HPF with a cutoff wavelength of 4 min was applied to the ΔH among observatories ORC, PST and KEP. Oscillations with an amplitude between ±0.2 and 0.5 nT, occurring approximately 6 hours before the earthquake on June 29, 2014, are shown (Figure 10a). The filtering shows two periods of significant amplitudes for 10 and 20 minutes, separated by 15 minutes, which are similar to the duration interval of the series of earthquakes occurring with the event on June 29, 2014. The filtering of the earthquakes on August 12, 2021 shows maximum oscillations of ± 0.2 nT, 2.5 hours before and for a period of 1.5 hours before the occurrence of ten earthquakes (M_w 5 to 8.1), which were chained together every 2 to 3 minutes after the first one (M_w 7.5). These results are consistent with the results yielded by the continuous wavelet transform (Figure 10b).

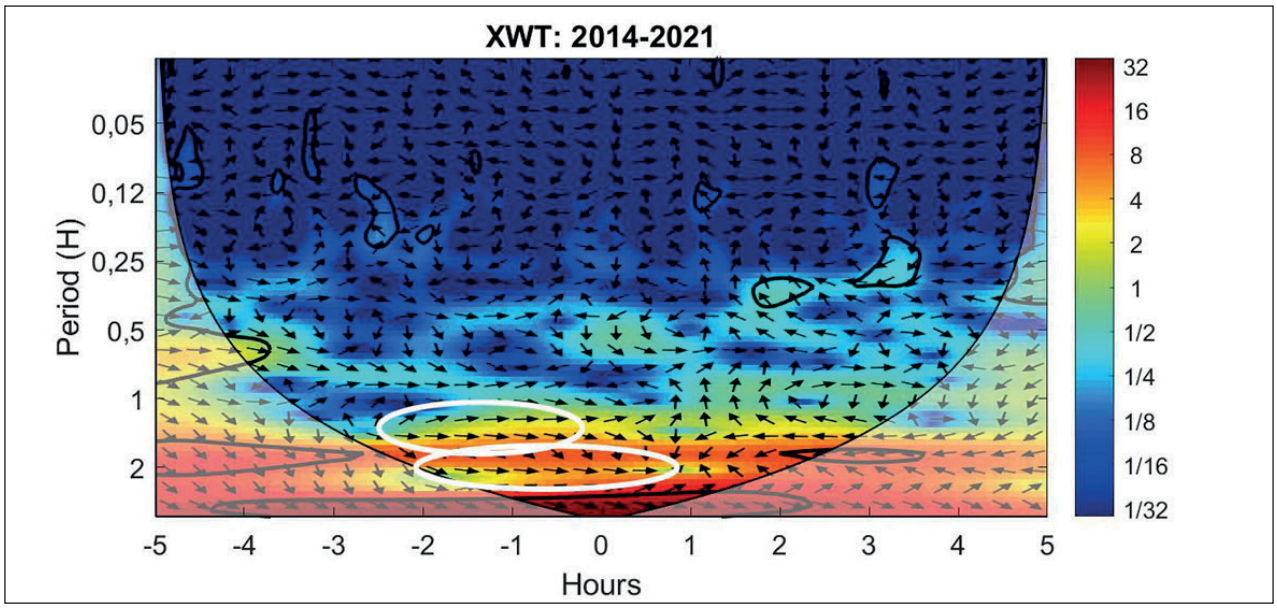

Figure 9. Crossed wavelet correlation (XWT) centered on the earthquake, between the events on June 29, 2014 and August 12, 2021. High significance level (black curves). Direct correlation (white ovals). COI edge effects (blurry image).

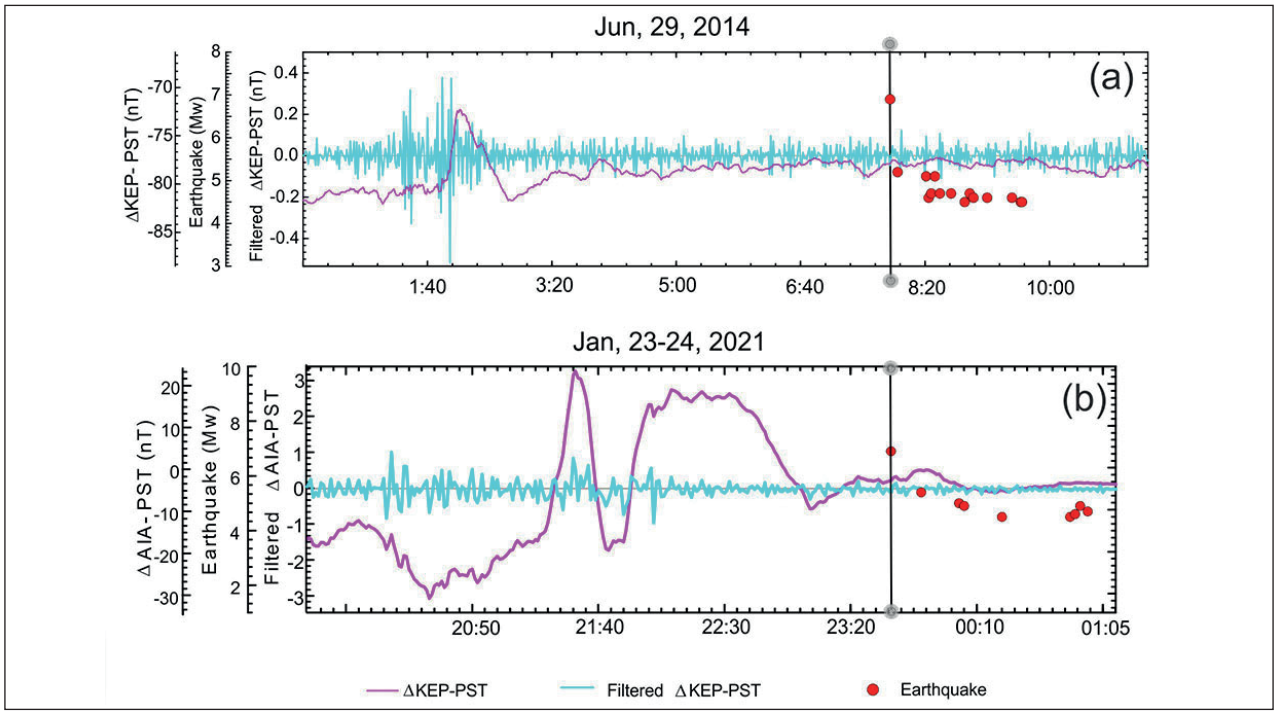

Figure10. Difference of the H component of the magnetic field between observatories (ΔH) (magenta line). Filtered ΔH (cyan line). Earthquake (red dot). (a) ΔKEP-PST June 29, 2014; (b) ΔKEP-PST August 12, 2021.

Unlike in the South Scotia Ridge area, in this region there is WL information available for 6 $M_w \geq 7$ events, of which only those occurring on December 11, 2018 (M_w7.1) and August 12, 2021 (M_w8.1) are shown (Figures 11a and b).

In the events occurring on June 30, 2008 (M_w7.0), July 15, 2013 (M_w7.3), May 28, 2016 (M_w 7.2) and August 22, 2021 (M_w7.1), the effect of the earthquake on the WL is not clearly identified, except for, in some cases, small variations below 0.10 m, which may suggest its occurrence, but are not conclusive as they may be due to other phenomena.

The duration of the water surface disturbance may be identified with greater amplitudes at the stations, without exceeding, in any case, two days from the occurrence of the earthquake on December 11, 2018 780 km away from KE and 1900 km away from BP (Figure 11a). By contrast, the event occurring on August 12, 2021 does allow for the clear identification of the earthquake effect on the WL variation in nearly all the stations analyzed, and the time of arrival of the tsunami at each station can also be calculated. The tsunami amplitudes vary according to the station analyzed, from values around 1.3 m at KE to values around 0.10 m at PM or MP (Figure 11b).

Figure 12 shows the space-time analysis of the sea-level pressure behavior in the area of the convergent margin on June 29, 2014, between 7:00 and 9:00 (UTC), and on August 12, 2021, between 18:00 and 19:00 (UTC). Around the

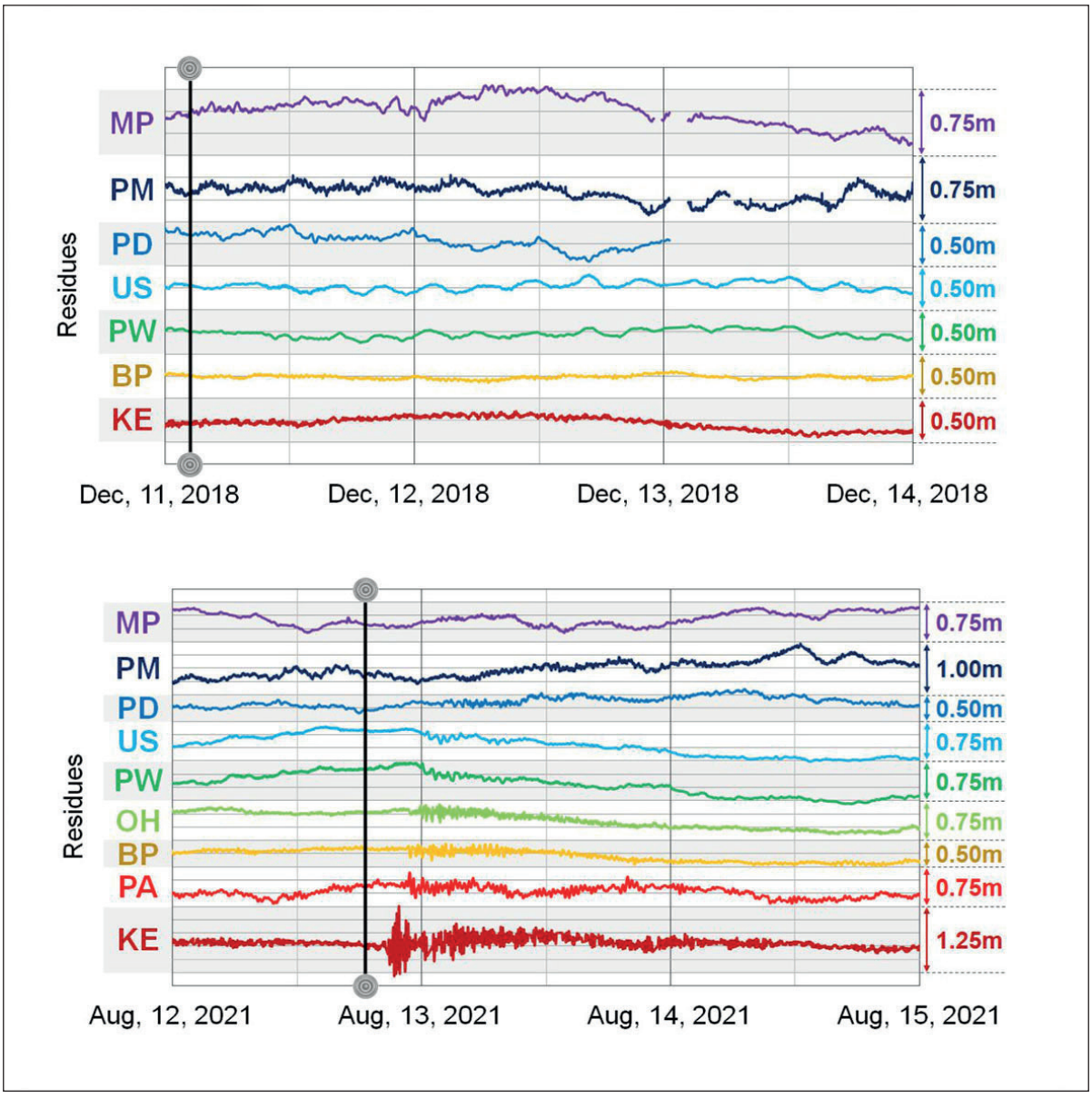

Figure 11. WL measurement from tide stations King Edward (KE), Puerto Argentino (PA), Base Prat (BP), O'Higgins (OH), Puerto Williams (PW), Ushuaia (US), Puerto Deseado (PD), Puerto Madryn (PM) and Mar del Plata (MP): (a) after the earthquake on December 11, 2018 (M_w7.1) at 02:26 (UTC), at a depth of 133 km; (b) after the earthquakes of August 12, 2021 (M_w7.5 and M_w8.1) at 18:32-18:35 (UTC), at a depth of 47 and 55 km, respectively. Event (black vertical line).

earthquake epicenter (gray bar), an area of disturbance in the isobars and pressure variation in the time series can be seen. Throughout the area, the isobar pattern is not uniform. Table 3 shows the period and magnitude of this variation for each event analyzed.

Figure 12a shows a non-uniform isobar distribution pattern, coinciding with great seismic activity due to the occurrence of 7 earthquakes (between M_w4.4 and 6.6) in a period not longer than one hour within 50 km from the area studied. It is a set of superficial earthquakes occurring at a depth of 8-10 km.

In addition, the pressure variation at the earthquake epicenter is altered when it increases (Figure 12c). Figure 12b shows an irregular isobar distribution pattern associated with the M_w7.5 and M_w 8.1 earthquakes resulting from a reverse fault sharply dipping northwestwards in the subduction area of the Scotia Arc, at a depth of ~56 km and 47 km, respectively. The earthquakes occurred with a difference of 3 minutes and at a distance of ~90 km. It should be noted that, within 30 minutes after 18:32, there was a series of earthquakes with a considerable magnitude aligned to the convergent margin that may have caused the pressure to drop from 18:30 to 21:30 (Figure 12d).

North Scotia Ridge

In this area, two earthquakes occurred on November 25, 2013 (M_w7.0) and on August 19, 2016 (M_w 7.4) at a depth of 11.8 and 10 km, respectively. The former was considered as a significant earthquake by the USGS.

We observed that the earthquakes on November 25, 2013, close to Malvinas (PST), and on August 19, 2016, close to KEP, even though they occurred at the same depth (~10 km)

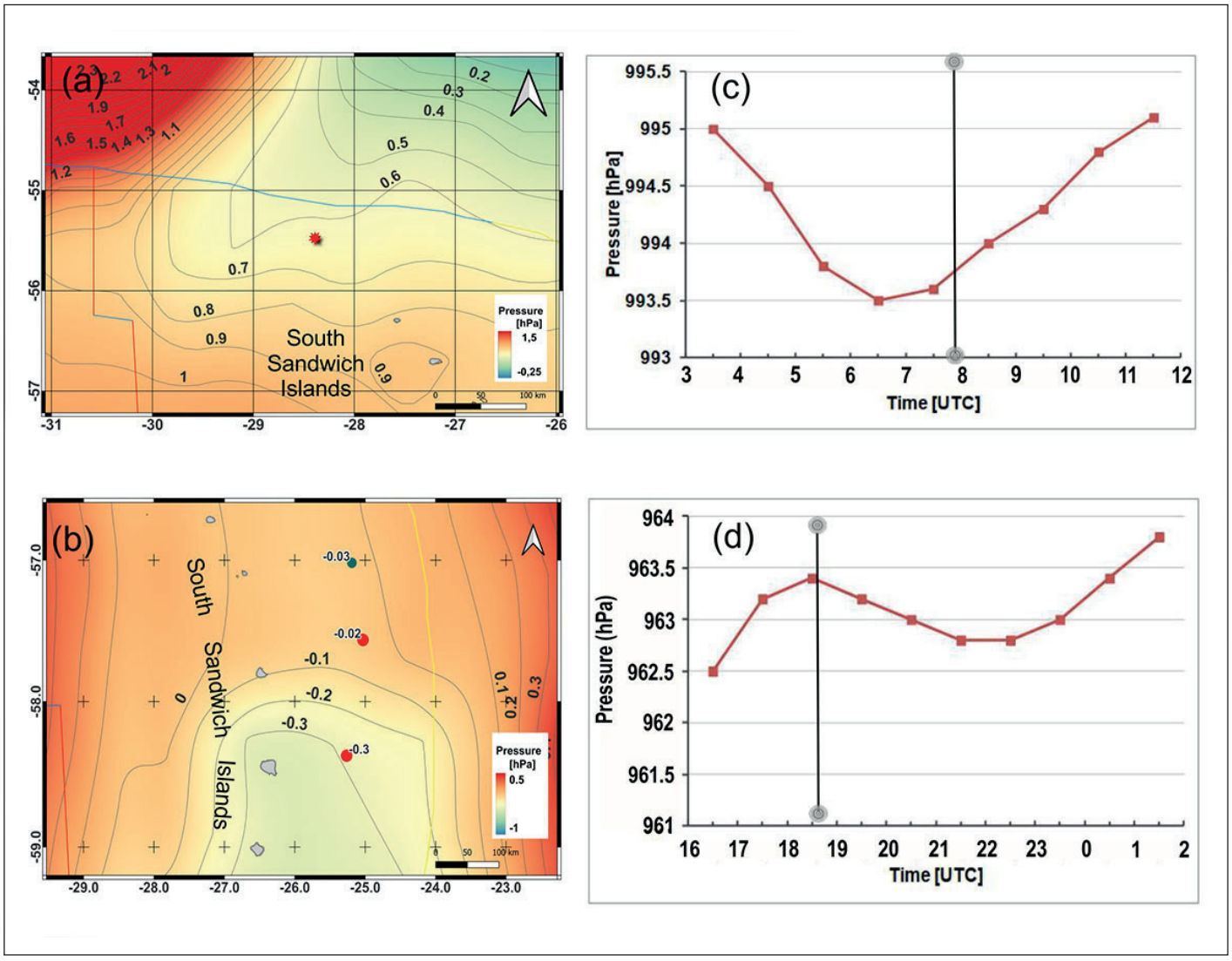

Figure 12. Differences of ocean-level AP grids on: (a) June 29, 2014 (7:00-9:00); (b) August 12, 2021 (18:00-19:00). Time series of sea-level hourly AP: (c) June 29, 2014 (3:30-11:30); (d) August 12-13, 2021 (16:30-1:30). Plate margins: divergent margin (red line): convergent margin (yellow line); transcurrent margin (blue line). Earthquakes: position according to the coordinates of their epicenter (left) (red dots). Local difference (green dots); time location (right) (gray bar).

and on the same type of margin, do not show common frequencies in the wavelet analysis. Because of this, no results can be obtained from the cross correlation.

The HPF does not allow for the identification of anomalous oscillations before the earthquake on November 25, 2013. Nevertheless, for the earthquake on August 19, 2016, the filter shows oscillations of ± 0.4 nT to 0.2 nT, around 3 hours before its occurrence, separated by 30 minutes in a consistent manner with a period of 22 minutes separating the 5 earthquakes that occurred after the earthquake studied (Figure 13).

In the North Scotia Ridge area, there are WL recordings for only 2 $M_w \geq 7$ events on November 25, 2013 (M_w7) and on August 19, 2016 (M_w7.4), which are shown on Figure 14. The WL behavior at the stations analyzed does not allow for a clear identification of the effect of either earthquake, except for KE, where a small disturbance below ±0.30 m about 8 hours and 30 minutes later, 1200 km and 290 km away, respectively, could be attributed (Figure 14a and b). The behavior in this area is similar to the one observed in the previous ones for earthquakes with similar magnitudes, not posing a risk for coastal populations.

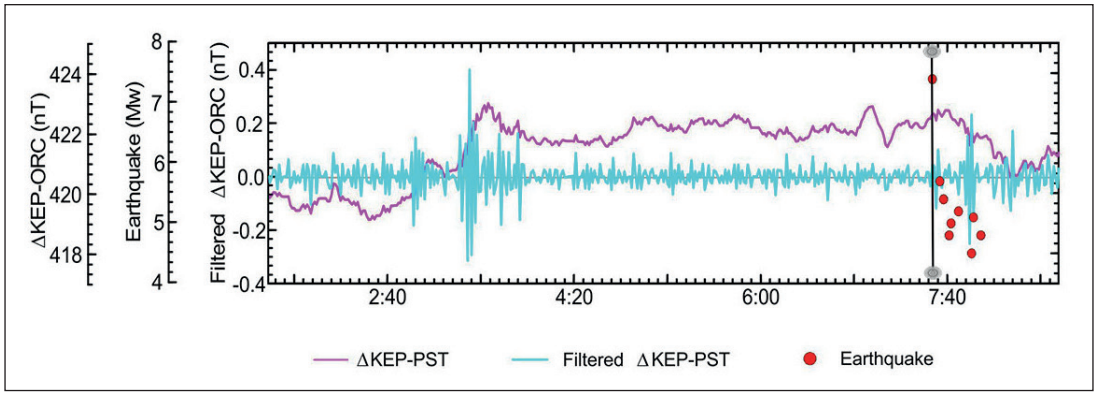

Figure 13. Difference of the H component of the magnetic field between observatories (ΔH) (magenta line). Filtered ΔH (cyan line). Earthquake (red dot). For ΔKEP- ORC: August 19, 2016.

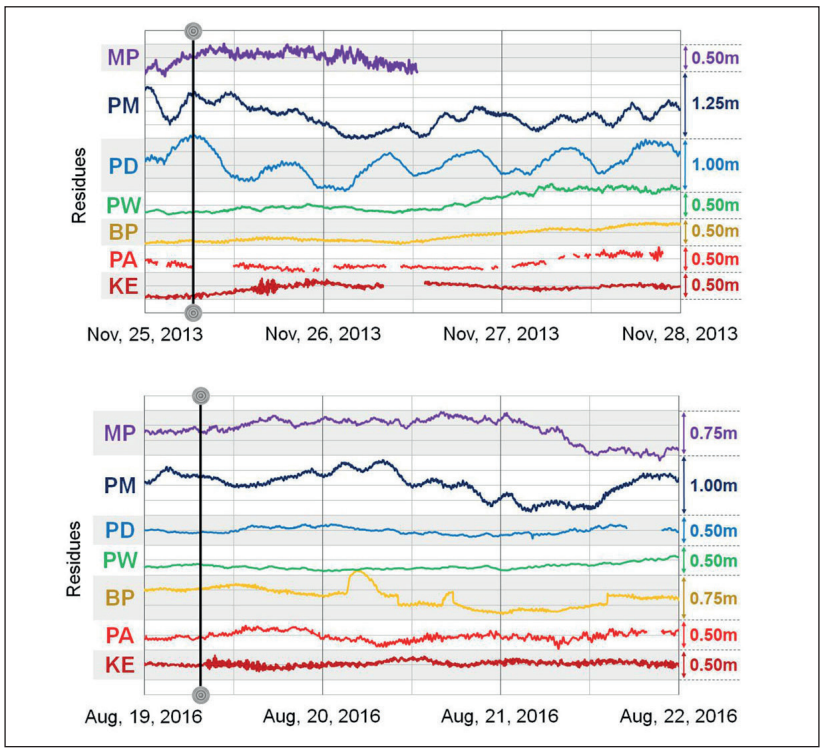

Figure 14. WL measurement from tide stations King Edward (KE), Puerto Argentino (PA), Base Prat (BP), O'Higgins (OH), Puerto Williams (PW), Ushuaia (US), Puerto Deseado (PD), Puerto Madryn (PM) and Mar del Plata (MP): (a) after the earthquake on Nov 25, 2013 (M_w 7) at 6:27 (UTC) at a depth of 11.8 km; (b) after the earthquake on August 19, 2016 (M_w7.4) at 7:32 (UTC), at a depth of 10 km. Event (black vertical line).

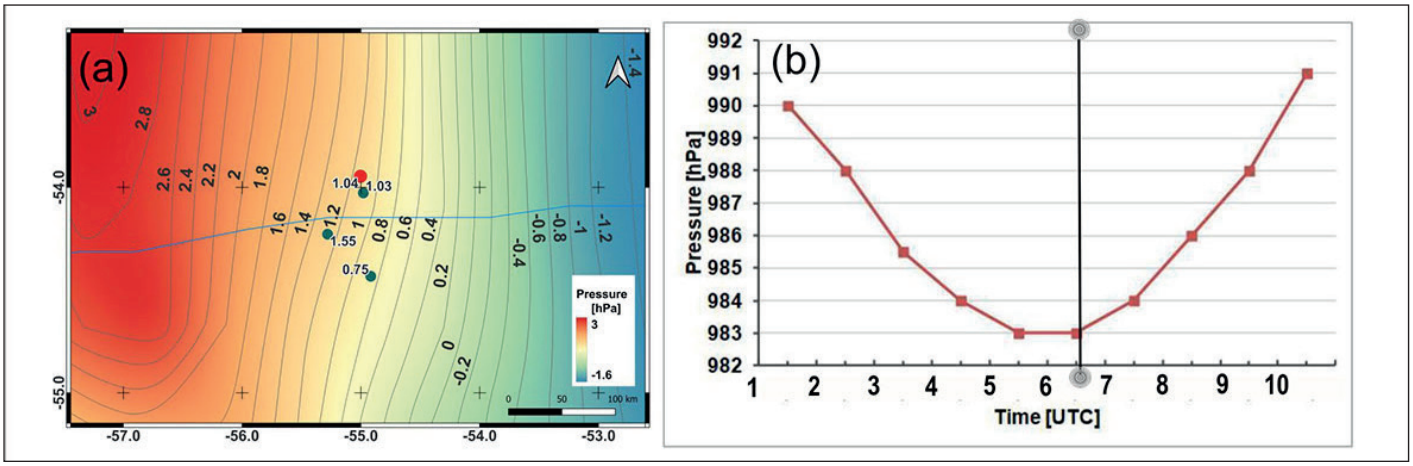

Figure 15. Differences of ocean-level AP grids on: (a) November 25, 2013 (5:00-7:00). Time series of sea-level hourly AP: (b) November 25, 2013 (1:30-10:00). Plate margins: transcurrent margin (blue line). Earthquakes: position according to the coordinates of their epicenter (left) (red dot). Local difference (green dots); time location (right) (gray bar).

Figure 15 shows the results of the space-time analysis of the sea-level pressure behavior in this area for the event on November 25, 2013 between 5:00 and 7:00 (UTC). A behavior pattern that appears to be different from the previous ones can be distinguished with regard to the transcurrent margin. Nevertheless, around the earthquake epicenter, an area of disturbance in isobars and pressure variation in the time series can be seen. This behavior can be seen in the grid (Figure 15a) by means of the concave curvature towards the location of the M_w7 earthquake, which is consistent with the fault strike (SSW) evidenced by the alignment of five earthquakes (from M_w 4.9 to 5.6) occurring in a period of 10 minutes after the earthquake under study (Figure 15a). In addition, the time pressure recording, measured at the location of the earthquake (1:30 – 10:06), shows a change in tendency. While some hours before the event the pressure tends to drop, some hours later it increases. Table 3 shows the period and magnitude of this variation for each event analyzed.

Study of medium and low GMF frequencies

It was found that 70% of the ΔH analyzed 24 hours before and after the earthquakes studied showed medium to low frequencies with an anticipation of 12 to 4 hours, while only 10% showed an anticipation in a range below 4 hours, and 20% did not show any frequency whatsoever. In some cases, an alteration in low to medium frequencies could be found after their occurrence; 20% in a range of 0 to 4 hours and 30% in a range of 4 to 12 hours. No typical frequencies could be observed after the earthquakes in 50%. Table 4 displays the data recorded.

Table 4. Compilation of frequencies from the Continuous Wavelet Transform analysis before and after the earthquakes on disturbed days.

Date and time	Frequencies (Hz)	Depth (km)	Mag (M_w)	Disturbed day	Anticipation period (hs)	Delay period (hs)
2003/08/04; 4:37	0.004 to 0.26	10	7.6	No	6	8
2006/01/02; 6:10	0.004 to 0.03	13	7.4	No	6	No
2006/08/20; 3:41		13	7	No	0-12	0-12
2008/06/30; 6:17	0.004 to 0.266	8	7	No	0-8	0-8
2013/07/15; 14:03		11	7.3	No	0-4	0-4
2013/11/17; 9:04		10	7.7	No	3-4	3-4
2013/11/25; 6:27	0.001 to 0.002	11.8	7	No	No	No
2014/06/29; 7:52		8	6.9	No	4-5	No
2016/05/28; 9:46		78	7.2	No	4-8	8
2016/08/19; 7:32	0.004 to 0.033	10	7.4	No	No	No
2018/12/11; 2:26		133	7.1	Yes	No	No
2019/08/27; 23:55		11.8	6.6	No	1-2	1-2
2021/01/23; 23:36		9.8	6.9	No	3-7	No
2021/08/12; 18:32		55.7	7.5	No	1-2	1-2
2021/08/12; 18:36	0.004 to 0.033	14	8.1	No	1-2	1-2
2021/08/22; 21:33		47.2	7.1	No	6	No

Conclusions

It is possible to distinguish different responses of the GMF, WL and AP according to the type of margin where the seismic event occurs.

It is possible to detect anomalous variations in geomagnetic field records in spans from 1 to 12 hours before and after the manifestation of seismic events with a magnitude above M_w6.6. By means of a high-pass filter, anomalous peaks with amplitudes of up to ±0.4nT were recognized on the geomagnetic signals of ΔH with an anticipation of up to 6 hours and durations compatible with the results of the continuous wavelet transform and the series of earthquakes occurring with the $M_w \geq$ 6.6 earthquake. In the WL residues, amplitudes of up to ±0.3m and compatible arrival times were detected according to the distance from the tide sensor to the earthquake. The isobar distribution pattern was consistent with the fault planes of the earthquakes.

In the South Scotia Ridge, the geomagnetic field showed anomalies in ranges from 3 to 5 hours before the seismic activity. In addition, there were anomalous WL values in the sensors closest to the events with amplitudes of ~ 0.30 m. The cases analyzed do not necessarily represent the behavior of the WL variation of earthquakes occurring in this area, but, as the occurrence frequency and magnitude is one of the most significant in the region, they may be considered as a first indicator of the amplitude expected on nearby shores. Additionally, isobars can have AP anomalies of up to 0.3 hPa at the earthquake epicenter.

In the plate subduction area, the geomagnetic field study did not highlight the greatest magnitude earthquake (M_w8.1) due to a series of earthquakes occurring in less than three minutes, even though it made it possible to observe the typical low frequencies due to the plate friction. In addition, the filters showed even amplitudes during the 5-hour period studied without yielding specific and identifiable frequencies. Similarly, the isobar distribution was very irregular. After the M_w 8.1 earthquake, the WL residues showed disturbances at most stations; only at King Edward amplitudes reached 1.30 m. Although it did not pose a potential risk, even when combined with storm surge events, like in Puerto Madryn and Mar del Plata, and given its significant magnitude, it may be considered as a first indicator of the amplitude expected on nearby shores in the region.

The transcurrent margin of the North Scotia Ridge showed a low response of the geomagnetic field to the presence of seismic activity. Nevertheless, there are anomalous variations in the WL at close tide stations (0.10 m), as well as 0.3 hPa atmospheric pressure variations both in isobars and the time series after the seismic activity. The WL behavior in this area is similar to the behavior of previous ones for earthquakes with similar magnitudes, not posing a risk for coastal populations as long as the same depth characteristics are maintained.

Results vary according to the area under study as the tectonic characteristics of the margins of the Scotia and Sandwich plates yield different results of geomagnetic signals. The selection of earthquakes in three areas with different characteristics leads us to think that results largely depend on their tectonogenesis. They either make it possible to see frequencies or not, based on their particular characteristics. This is worthy of a more thorough and detailed analysis to be addressed in future research.

Moreover, given that one of the magnitudes to study was the GMF that is affected by solar activity, it was proposed to evaluate periods of solar activity, based on the number of sunspots, in comparison with the 23 selected earthquakes, concluding that more than a half of the earthquakes occurred in the period of decrease or minimum of solar activity.

Acknowledgements

We thank the referees for their valuable comments. This study was partly subsidized by projects UNDEFI No. 259/2020 and UBACyT 20020190100236BA.

References

Arai N., Iwakuni M., Watada S., Imanishi Y., Murayama T. and Nogami M., (2011). Atmospheric boundary waves excited by the tsunami generation related to the 2011 great Tohoku-Oki earthquake, *Geophys. Res. Lett., 38*, L00G18. **https://doi.org/10.1029/2011GL049146**.

Ayca, A., & Lynett, P. J., (2016). Effect of tides and source location on nearshore tsunami-induced currents. *Journal of Geophysical Research: Oceans,121*, n8807– 8820. **https://doi.org/10.1002/2016JC012435** 2011GL049146.

Arecco, M.A. Larocca P.A., Mora M.C., (2020). Geomagnetismo y su relación con sismos. Un estudio en la microplaca de Sandwich del Sur, *Revista Defensa Nacional*, v 4, 263-281. **http://www.cefadigital.edu.ar/handle/1847939/1558**.

Banegas L., Grismeyer W.H., Fiore M.M.E., Oreiro F.A., (2021). Actualización de la interfase para la descarga de datos de marea Publicados por la Comisión Oceanográfica Intergubernamental Informe Técnico Nº 04/21. Departamento Oceanografía del Servicio de Hidrografía Naval, 12p.

Beniest A., Schellart W.P., (2020). A geological map of the Scotia Sea area constrained by bathymetry, geological data, geophysical data and seismic tomography models from the deep mantle, Earth-Science Reviews, Volume 210, 103391. **https://doi.org/10.1016/j.earscirev.2020.103391**.

Dalziel I.W.D., Lawver L.A., Norton I.O. and Gahagan L.M., (2013). The Scotia Arc: Genesis, Evolution, Global Significance. *Annual Review of Earth and Planetary Sciences 41:* 767–793. **https://doi.org/10.1146/annurev-earth-050212-124155**.

Dragani, W. C., D'Onofrio, E. E., Grismeyer, W., Fiore, M. M., Violante, R. A., and Rovere, E. I., (2009). Vulnerability of the Atlantic Patagonian

coast to tsunamis generated by submarine earthquakes located in the Scotia Arc region. Some numerical experiments. *Natural hazards, 49*(3), 437-458. **https://doi.org/10.1007/s11069-008-9289-4**.

Eagles G., (2010). The age and origin of the central Scotia Sea. *Geophysical Journal International 183:* 587–600. **https://doi.org/10.1111/j.1365-246X.2010.04781.x**.

Flanders Marine Institute (VLIZ), Intergovernmental Oceanographic Commission (IOC), (2021), *Sea level station monitoring facility.* VLIZ. **https://doi.org/10.14284/482**.

Gao, Y., Chen, X., Hu, H., Wen, J., Tang, J., and Fang, G., (2014), Induced electromagnetic field by seismic waves in Earth's magnetic field, *J. Geophys. Res. Solid Earth*, 119, 5651–5685, doi:10.1002/2014JB010962.

Gulyaeva, T. L., Arikan, F. E. Z. A., & Stanislawska, I. (2014). Probability of occurrence of planetary ionosphere storms associated with the magnetosphere disturbance storm time events. *Advances in Radio Science, 12*, 261-266.

Hayakawa, M., Kasahara, Y., Nakamura T., et al., (2010). A statistical study on the correlation between lower ionospheric perturbations as seen by subionospheric VLF/LF propagation and earthquakes, *Journal of Geophysical Research*, A, vol. 115, no. 9, Article ID A09305. **https://agupubs.onlinelibrary.wiley.com/doi/full/10.1029/2009JA015143**.

Jia, Z., Zhan, Z. and Kanamori, H., (2022). Earthquake: A Slow Event Sandwiched Between Regular Ruptures, *Geophysical Research Letters, 49*, (3). **https://doi.org/10.1029/2021GL097104**.

Kowalik, Z., and Proshutinsky, A., (2010). Tsunami–tide interactions: A Cook Inlet case study. *Continental Shelf Research*, 30, 633– 642. doi 10.1016/j.csr.2009.10.004.

Larocca, Patricia A.; Arecco, María A.; Mora, Mariana C., (2021). Wavelet-based Characterization of Seismicity and Geomagnetic Disturbances in the Sandwich del Sur Microplate Area. *Geofísica Internacional*. Vol 60, N°4, 320-332, **http://revistagi.geofisica.unam.mx/index.php/RGI/article/view/2119/1882**.

Larocca, P., Fiore, M., Oreiro F., Vilariño, I. and Arecco, M.A., (2019). Estudio de parámetros geomagnéticos y su posible influencia sobre anomalías sismo-ionosféricas. In Proceedings of the Sixth Biennial Meeting of Latinmag, Fernando Poblete, C. I. Caballero M, (Eds), Latinmag Letters, 9, Special Issue, Proceedings A18, 1-6, Rancagua, Chile. **https://www.geofisica.unam.mx/LatinmagLetters/LM19-0101SP/A-P/A.18-P.pdf**.

Leat P.T., Day S.J., Tate A.J., Martin T.J., Owen M.J. and Tappin D.R. (2013). Volcanic evolution of the South Sandwich volcanic arc, South Atlantic, from multibeam bathymetry. *Journal of Volcanology and Geothermal Research 265*: 60–77. **https://www.sciencedirect.com/science/article/abs/pii/S0377027313002552**.

Leat P., Fretwell P., Tate A., Larter R., Martin T., Smellie J., Jokat W. and Bohrmann G. (2016). Bathymetry and geological setting of the South Sandwich Islands volcanic arc. *Antarctic Science 28* (4), 293-303. doi:10.1017/S0954102016000043.

Lee, H. S., Shimoyama, T., & Popinet, S. (2015). Impacts of tides on tsunami propagation due to potential Nankai Trough earthquakes in the Seto Inland Sea, Japan. *Journal of Geophysical Research*: Oceans, 120, 6865– 6883. **https://doi.org/10.1002/2015JC010995**.

Maldonado A., Dalziel I. and Leat P.T. (2013). Understanding the evolution of the Scotia arc. *EOS 94*: 272–272. **https://agupubs.onlinelibrary.wiley.com/doi/pdf/10.1002/2013EO310004**.

Maldonado A., Dalziel I.W.D. And Leat P.T. (2015). The global relevance of the Scotia Arc: An introduction. *Global and Planetary Change 125*: 1–8.

Paudel, S. R., Banjara, S. P., Wagle, A., & Freund, F. T. (2018). Earthquake chemical precursors in groundwater: a review. *Journal of Seismology, 22*(5), 1293-1314. **https://link.springer.com/article/10.1007/s10950-018-9739-8**.

Rabinovich, A. B. (2010). Seiches and harbor oscillations. In Handbook of coastal and ocean engineering (pp. 193-236). **https://doi.org/10.1142/9789812819307_0009**.

Roucco M.I. and Del Valle, R. A. (2021, 12 de julio). Tsunami tectónico en las islas Orcadas del Sur de la Antártida Argentina. Fundación Marambio. **https://www.marambio.aq/tsunamiorcadas.html**.

Ruiz, F., Sánchez, M., Martínez. P., Giménez, M., Leiva, F., Álvarez, O., Introcaso, A. (2011). La estación magnética Zonda: estudio de perturbaciones magnéticas relacionadas con terremotos. San Juan, Argentina. Proceedings of Second Biennial Meeting of Latinmag, Special Issue, A.M. Sinito (Ed.), Latinmag Letters, Vol. 1, Special Issue, A16, 1-7. **https://www.geofisica.unam.mx/LatinmagLetters/LL11-0102P/A/A16-Ruiz-corregido.pdf**.

Shelby, M., Grilli, S. T., and Grilli, A. R. (2016). Tsunami hazard assessment in the Hudson River Estuary based on dynamic tsunami-tide simulations. *Pure and Applied Geophysics, 173* (12), 3999 – 4037. **https://doi.org/10.1007/s00024-016-1315-y**.

Sierra Figueredo, P., Mendoza Ortega, B., Pazos, M. et al. (2021). Schumann Resonance anomalies possibly associated with large earthquakes in Mexico. *Indian J Phys 95*, 1959–1966. **https://doi.org/10.1007/s12648-020-01865-6**.

Spivak, A. A., & Riabova, S. A. (2019). Geomagnetic variations during strong earthquakes. Izvestiya, *Physics of the Solid Earth, 55*(6), 811-820. **https://link.springer.com/article/10.1134/S1069351319060077**.

Takahashi, S., T. Iyemori y M. Takeda (1990). Ring current response to impulsive southward IMF: A cause of second development of the Dst index, *J. Geomag. Geoelectr., 42*, 1325-1331. **https://www.jstage.jst.go.jp/article/jgg1949/42/11/42_11_1325/_pdf**.

Takeuchi, A. Okubo, K., Takeuchi, N. (2012). Electric Signals on and under the Ground Surface Induced by Seismic Waves, *International Journal of Geophysics Volume 2012*, Article ID 270809, 10 pages, doi:10.1155/2012/270809.

Takla E., A. Khashaba, Abdel Zaher M., Yoshikawa A. and Uozumi T. (2018). Anomalous ultra-low frequency signals possibly linked with seismic activities in Sumatra, Indonesia. NRIAG *Journal of Astronomy and Geophysics, 7*:2, 247-252. doi: 10.1016/j.nrjag.2018.04.004.

Thomas H.J. and Juarez A. (2021). Stress–strain characterization of seismic source fields using moment measures of mechanism complexity, *Geophysical Journal International*, Volume 227, Issue 1, October 2021, Pages 591–616, **https://doi.org/10.1093/gji/ggab218**.

Varotsos P. A., Sarlis N.V., Skordas E.S., Lazaridou M.S. (2013). Seismic Electric Signals: An additional fact showing their physical interconnec-

tion with seismicity, Tectonophysics, Volume 589, 116-125. **https://www.sciencedirect.com/science/article/pii/S0040195113000024**.

Woodworth, P. L., Pugh, D. T., Meredith, M. P., and Blackman, D. L. (2005). Sea level changes at Port Stanley, Falkland Islands. *Journal of Geophysical Research: Oceans, 110* (C6). **https://agupubs.onlinelibrary.wiley.com/doi/full/10.1029/2004JC002648**.

Zhao, J., Gao, Y., Tang, J., Klemperer, S. L., Wen, J., Chen, C.-H., and Chong, J. (2021). Electromagnetic field generated by an earthquake source due to motional induction in 3D stratified media, and application to 2008 M_w 6.1 Qingchuan earthquake. *Journal of Geophysical Research: Solid Earth, 126*, e2021JB022102. **https://doi.org/10.1029/2021JB022102**.